P4.7 Impact of MODIS BRDF and Albedo on Land Surface Models

Zhuo Wang*, Xubin Zeng, and Michael Barlage
Institute of Atmospheric Physics, University of Arizona, Tucson, AZ85721

Robert Dickinson
School of Earth and Atmospheric Sciences, Georgia Institute of Technology, Atlanta, GA30332

Crystal Schaaf, and Feng Gao
Department of Geography, Boston University, Boston, MA02215

1. Introduction

Land surface albedo describes the fraction of incoming solar energy reflected at a given point and time, and hence determines the surface temperature and evapotranspiration. It is strongly dependent on the solar zenith angle and the three-dimensional structure of vegetation canopy (e.g., Yang et al. 2001; Schaaf et al. 2002). The land surface albedo in regional and global models can be specified using empirical observations or computed based on a radiation submodel for canopy plus underlying soil. These approaches do not consider the three-dimensional structure of vegetation.

To evaluate and improve model treatment of surface albedo, Li and Garand (1994) used Earth Radiation Budget Experiment (ERBE) measurements to derive surface albedo (2.5° × 2.5°) from the top of atmosphere albedo. Csiszar and Gutman (1999) and Strugnell et al (2001) produced nadir surface albedos from the Advanced Very High Resolution Radiometer (AVHRR) data. Wei et al. (2001) used the latter to evaluate the albedos of two land surface models: the Biosphere-Atmosphere Transfer Scheme (BATS) (Dickinson et al. 1993) and the National Center for Atmospheric Research (NCAR) Land Surface Model (LSM; Bonan 1996). They found that the models display a high bias as compared to the satellite observation in desert and semidesert regions. Both models also demonstrate a high bias over regions of winter snow. More recently, the Moderate Resolution Imaging Spectroradiometer (MODIS) Bidirectional Reflectance Distribution Function (BRDF) and albedo data become available (Schaaf et al. 2002). The MODIS albedo data are of much better quality than the AVHRR data (Justice et al. 2002; Guenther et al. 2002; Wolfe et al. 2002). In particular, the MODIS BRDF data enable us to better evaluate the solar zenith angle dependence of surface albedo.

Zhou et al. (2003) have used the MODIS albedo data to evaluate the land surface albedo from the Common Land Model (Zeng et al. 2002) and explored the reasons for the differences. Oleson et al. (2003) have also used the MODIS data to preliminarily evaluate the local-noon direct albedo of the NCAR Community Climate System Model (CCSM2; Blackmon et al. 2001). Parallel with and complementary to these efforts, here we intend to evaluate the solar zenith angle dependence of albedo in the CCSM2 as well as model monthly averaged albedo and direct solar beam albedo at local noon using the MODIS BRDF data. These studies as well as the MODIS BRDF/albedo data will also provide a good starting point towards the development of a BRDF-based treatment of radiative transfer within canopy for regional and global models.

2. Model albedo and MODIS BRDF/albedo data

2.1 Model albedo

The CCSM2 albedo is computed in its land surface component, that is, the Community Land Model (CLM2; Bonan et al. 2002b) which is primarily from the Common Land Model (CLM; Zeng et al. 2002; Dai et al. 2003). The albedo at each time step consists of four components: direct and diffuse

---

* *Corresponding author address*: Zhuo Wang, Univ. of Arizona, Institute of Atmospheric Physics, 1118 E., 4th St., Tucson, AZ 85721-0081; e-mail: zhuowang@atmo.arizona.edu

albedos for the visible (with wavelength $\lambda < 0.7\,\mu m$) and near-infrared (with $\lambda > 0.7\,\mu m$) bands. The monthly averaged total (i.e., direct plus diffuse) reflected and incoming solar radiation fluxes are standard CCSM2 output, and their ratio is referred to as the monthly averaged model albedo (Monteith 1973). This corresponds to the energy-weighted temporal average of instantaneous albedos.

To evaluate the solar zenith angle dependence of model albedo, we have also run the simulation using CLM2 coupled with the Community Atmospheric Model (CAM2) (which is the atmospheric component of CCSM2) along with sea surface temperature and sea ice specified based on observational data.

Both CCSM2 and CAM2/CLM2 have a horizontal resolution of 2.8° × 2.8° in the atmosphere. Each atmospheric grid cell over land is subdivided into up to five land cover types: glacier, lake, wetland, urban, and vegetation, which includes 1 – 4 of the 17 plant functional types (PFTs; including bare ground as one of the types, see Table 1; Bonan et al. 2002a). The fraction for each tile is specified and does not vary with time.

Table 1. Plant functional types (PFTs) as used in CLM2.

PFT	Description
0	Not vegetated
1	Needleleaf evergreen temperate tree
2	Needleleaf evergreen boreal tree
3	Needleleaf deciduous boreal tree
4	Broadleaf evergreen tropical tree
5	Broadleaf evergreen temperate tree
6	Broadleaf deciduous tropical tree
7	Broadleaf deciduous temperate tree
8	Broadleaf deciduous boreal tree
9	Broadleaf evergreen shrub
10	Broadleaf deciduous temperate shrub
11	Broadleaf deciduous boreal shrub
12	C3 Arctic grass
13	C3 Nonarctic grass
14	C4 Grass
15	Corn
16	Wheat

CLM2 separately computes albedos for soil, snow, and vegetation, and then takes the total albedo of a grid box (α) as an average of these albedos weighted by the representative area fractions:

$$\alpha = \alpha_s f_s + \alpha_{sn} f_{sn} + \alpha_v f_v \qquad (1)$$

where α refers to albedo, f refers to fraction, and the subscripts s, sn, and v stand for bare soil (and glacier, lake, and wetland, if their area fractions are greater than zero), snow, and vegetation, respectively. The summation of f_s, f_{sn}, and f_v should be equal to unity.

The snow albedo (α_{sn}) is a function of grain size, soot and solar zenith angle (Wiscombe and Warren 1980). The snow fraction (f_{sn}) includes the fractions of bare soil and vegetation covered by snow ($f_{sn,s}$ and $f_{sn,v}$, respectively). The value $f_{sn,s}$ depends on bare soil roughness length and snow depth (Dickinson et al. 1993), while $f_{sn,v}$ depends on snow intercepted by canopy and leaf and stem area indexes (Bonan et al. 2002b).

The soil albedo (α_s) is a function of prescribed soil color type and surface soil moisture but independent of solar zenith angle (Dickinson et al. 1993). The soil albedos for wavelength $\lambda > 0.7\,\mu m$ are assumed to be twice those for $\lambda < 0.7\,\mu m$ (Dickinson et al. 1993). Note that while this ratio (of two) is not unreasonable on average, it does vary geographically based on the recent MODIS data analysis over deserts (Tsvetsinskaya et al. 2002).

The vegetation albedo (α_v) for each PFT is obtained through the PFT-dependent leaf reflectance and transmittance, and through leaf orientation. These parameters are combined with soil albedo, leaf area index, and solar zenith angle by the two-stream approximation (Bonan 1996).

CLM2 is largely from the Common Land Model (CLM; Zeng et al. 2002; Dai et al. 2003). However, vegetation albedo in CLM2 is computed based on the two-stream approximation of Bonan (1996), while the method in CLM is closer to a single scattering approach under the constraint that canopy albedo approaches the product of the leaf area and the prescribed single scattering of individual leaves (or approaches the prescribed albedo for thick canopy) as leaf area index becomes small (or large). While the thick canopy albedo values in CLM [see Table 2 of Zeng et al. (2002)] are based on the AVHRR data analysis (Wei et al. 2001), the vegetation optical properties in CLM2 [see Table 4 of Bonan et al. (2002b)] are from a variety of sources (Dorman and Sellers 1989). Leaf and stem area indexes are required for the computation of vegetation albedo. Leaf area index data as used in CLM and CLM2 are from the AVHRR data. Stem area index is computed from the seasonal variation of LAI in CLM, and the seasonal variation of SAI in CLM2 is based on Bonan (1996).

2.2 MODIS data

The global 1-km MODIS BRDF/albedo data were derived by coupling all available cloud-free, atmospherically-corrected, spectral surface reflectance observations over a 16-day period with a semiempirical, kernel-driven BRDF model (Lucht et al. 2000a; Schaaf et al. 2002). The MODIS data are provided in three visible (460, 555, and 659 nm) and four near-infrared narrow bands (865, 1240, 1640, and 2130 nm), which are then used to infer the total shortwave ($0.3-5.0\,\mu m$), visible ($0.3-0.7\,\mu m$), and near-infrared ($0.7-5.0\,\mu m$) broadband albedos using the conversion coefficients in Liang et al. (1999).

Lucht et al. (2000a) employed the Ross-Li BRDF model with three parameters and kernels. The three parameters are an isotropic parameter (f_{iso}) (describing the nadir bidirectional reflectance at nadir illumination), a radiative transfer or volumetric scattering parameter (f_{vol}), and a surface scattering or geometric optics parameter (f_{geo}). The general form of the semiempirical model is a linear combination of kernels (Roujean et al. 1992; Schaaf et al. 2002):

$$\begin{aligned} R(\theta,\vartheta,\phi,\Lambda) = {} & f_{iso}(\Lambda) + f_{vol}(\Lambda) K_{vol}(\theta,\vartheta,\phi,\Lambda) \\ & + f_{geo}(\Lambda) K_{geo}(\theta,\vartheta,\phi,\Lambda) \end{aligned} \tag{2}$$

where $R(\theta,\vartheta,\phi,\Lambda)$ is the BRDF, θ is solar zenith angle, ϑ is view zenith angle, ϕ is view-sun relative azimuth angle, and Λ is wave band of width $\Delta\lambda$ (with λ being wavelength). The value K_{vol} is called the RossThick kernel for its assumption of a dense leaf canopy ($LAI >> 1$). It is a single-scattering approximation of radiative transfer theory by Ross (1981) consisting of a layer of small scatterers with uniform leaf angle distribution, a Lambertian background, and equal leaf transmittance and reflectance. The value K_{geo} is called the LiSparse kernel for its assumption of a sparse ensemble (no mutual shadowing permitted) of surface objects casting shadows on a Lambertian background.

Black-sky albedo (α_{bs}) is defined as the albedo in the absence of a diffuse component, and it is a function of solar zenith angle. White-sky albedo (α_{ws}) is defined as the albedo in the absence of a direct component, and it is independent of solar zenith angle. These two extremes can be combined as a function of the diffuse skylight fraction (S) for a representation of an actual albedo (Lucht et al. 2000a):

$$\alpha(\theta,\Lambda) = (1-S)\alpha_{bs}(\theta,\Lambda) + S\,\alpha_{ws}(\Lambda) \tag{3}$$

The solar zenith angle dependence of albedo can be adequately approximated by polynomials (Schaaf et al. 2002; Lucht et al. 2000a, b). The black-sky albedo is then

$$\begin{aligned} \alpha_{bs}(\theta,\Lambda) = {} & f_{iso}(\Lambda) + f_{vol}(\Lambda) h_{vol}(\theta) \\ & + f_{geo}(\Lambda) h_{geo}(\theta) \\ = {} & f_{iso}(\Lambda) + f_{vol}(\Lambda) \cdot (-0.007574 \\ & - 0.070987\theta^2 + 0.307588\theta^3) \\ & + f_{geo}(\Lambda) \cdot (-1.284909 - \\ & 0.166314\theta^2 + 0.041840\theta^3) \end{aligned} \tag{4}$$

where θ is the solar zenith angle, and h is a known polynomial of θ. The white-sky albedo is obtained by integrating the black-sky albedo over all solar zenith angles:

$$\begin{aligned} \alpha_{ws}(\Lambda) = {} & \int_{\theta=0}^{\pi/2} \alpha_{bs}(\theta,\Lambda)\, d\left(\sin^2\theta\right) \\ = {} & f_{iso}(\Lambda) + 0.189184 f_{vol}(\Lambda) \\ & - 1.377622 f_{geo}(\Lambda) \end{aligned} \tag{5}$$

Equations (4) and (5) are used to obtain the black-sky and white-sky albedos for each band. Finally these results are converted to the visible

($0.3-0.7\,\mu m$), near-infrared ($0.7-5.0\,\mu m$), and shortwave ($0.3-5.0\,\mu m$) broad band albedos using the empirical spectral-to-broad band conversion coefficients (Liang et al. 1999).

Satellite remote sensing provides a broad view of surface albedos due to its large spatial scale and coverage, but various factors complicate the retrieval of surface albedo from such measurements. Corrections are required for atmospheric effects in estimating surface albedo from satellite measurements made above the atmosphere. Remotely sensed data depend on the view and solar angles (i.e., the surface is not Lambertian), and thus BRDF must be used to reconstruct the albedo. In addition, narrow spectral albedos must be transformed to match the broad band used by climate models. Errors arise and may accumulate at each of the above steps. To partially address these limitations, the MODIS data also include flags to indicate the confidence level of the BRDF/albedo data. In contrast, such flags were not available for the AVHRR albedo data (e.g., Csiszar and Gutman 1999).

3. Evaluation of CCSM2 monthly averaged albedo

The standard output from most global climate models includes monthly averaged reflected and incoming solar radiation fluxes at surface, and their ratio is defined as the monthly averaged albedo. This would be consistent with the MODIS albedo computed using Eq. (3) weighted by the incoming solar fluxes. However, diffuse skylight fraction (S) is not readily available, and Eq. (3) can not be directly used. Since the white-sky albedo (α_{ws}) represents the integration of the black-sky albedo over all solar zenith angles, it should be relatively close to the model albedo. Figures 1 and 2 compare February 2002 (MOD43C1, version 003) with the MODIS white-sky albedo from July 2001 and the CCSM2 climatological albedo for the same months (averaged over 10 yr). The quality flags indicate that the percentages of the MODIS data from full inversion are 49% in July (Fig. 1) and 33% in February (Fig. 2). If we only use the MODIS data over grid cells with full inversion, too much data would be eliminated. So, we decide to use all data with full/magnitude inversions, as in Oleson et al. (2003).

Figures 1 and 2 show that the overall spatial pattern of model albedo is consistent with that of the MODIS data. The model versus MODIS albedo differences are not statistically significant at the 95% level at 7.9% of the land grid cells between 60°S and 70°N in July (Fig. 1d) and at 18.9% in February (Fig. 2d). Furthermore, the albedo differences are within 0.02 in magnitude (which is the accuracy level of the MODIS data) at 38.1% of the land grid cells in July (Fig. 1d) and at 19.8% in February (Fig. 2d). The CCSM2 albedo is lower by 0.05-0.2 than the MODIS albedo over deserts in North Africa and Middle East. Since the model albedos over these deserts were prescribed largely based on the AVHRR data in Wei et al. (2001), these differences reflect the differences between the AVHRR and MODIS albedos to certain degree, with the latter more accurate (e.g., Tsvetsinskaya et al. 2002). The model albedo is also higher by more than 0.05 over parts of the South America, southern Africa, and Australia. Over Northern Hemisphere high latitudes, the model albedo in July is also higher by more than 0.05 (Fig. 1), as there is still (unrealistically) quite a bit of snow left in the model based on the distribution of the model snow water equivalent in July (figure not shown). Over snow-covered areas (e.g., the Northern Hemisphere high latitudes in February), Fig. 2 indicates a significantly higher model albedo than the MODIS data. In the completely snow-covered nonforested regions, this difference may be partially due to an error in the coefficients used to convert narrowband albedos to broadband albedos in situations of pure dry snow (Jin et al. 2002). This error, however, does not affect the MODIS albedo over the boreal zones (mixtures of snow and vegetation canopies). Note also that this artifact with respect to completely snow-covered regions is being rectified in the newer versions of the reprocessed MODIS data; however, we will focus on the snow-free areas only in this study.

In general, the difference field shown in Figs. 1c and 2c can be decomposed into two parts:

$$\begin{aligned}
&(CCSM2\ monthly\ averaged\ albedo) - \\
&(MODIS\ white-sky\ albedo) \\
&= [\,(CCSM2\ monthly\ averaged\ albedo) \\
&\quad -(MODIS\ average\ albedo)\,] + \\
&\quad [\,(MODIS\ average\ albedo) - \\
&\quad (MODIS\ white-sky\ albedo)\,]
\end{aligned} \tag{6}$$

where "MODIS average albedo" refers to the albedo computed using the MODIS BRDF/albedo data that

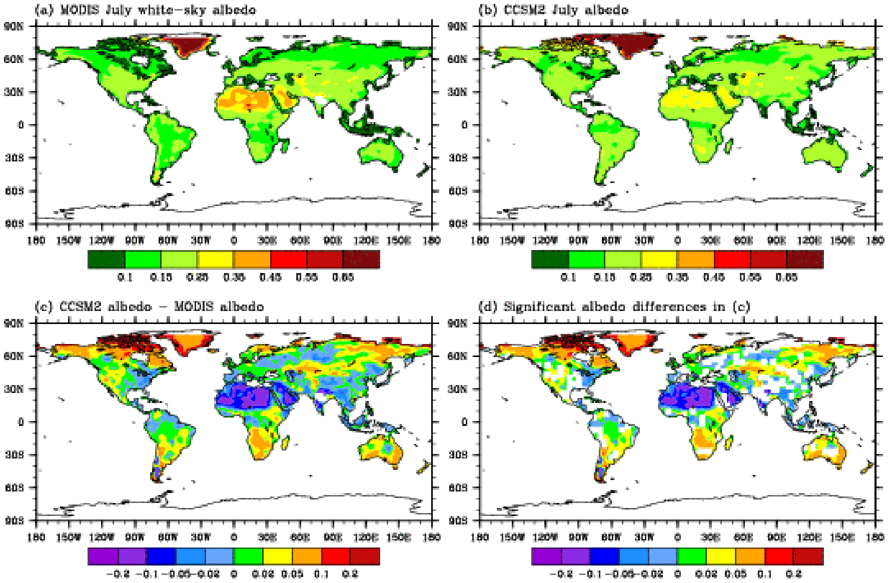

FIG. 1. The global distribution of land surface albedo in Jul. (a) MODIS white-sky albedo (α_{ws}) in 2001; (b) CCSM2 monthly albedo averaged over 10 yr; (c) CCSM2 albedo − MODIS α_{ws}; (d) significant (at 95 %) albedo differences in (c).

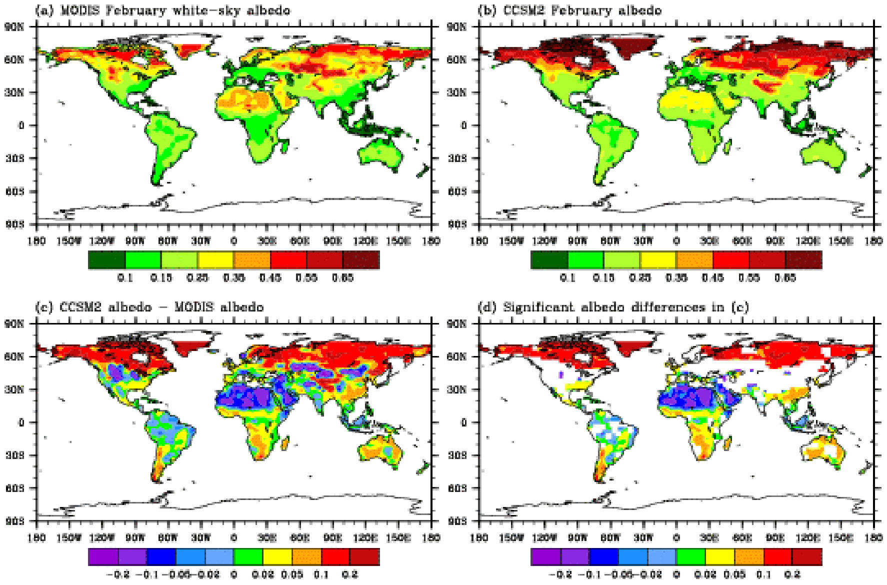

FIG. 2. Same as Fig. 1 except for Feb (MODIS data from Feb 2002 and model albedo averaged over 10 yr).

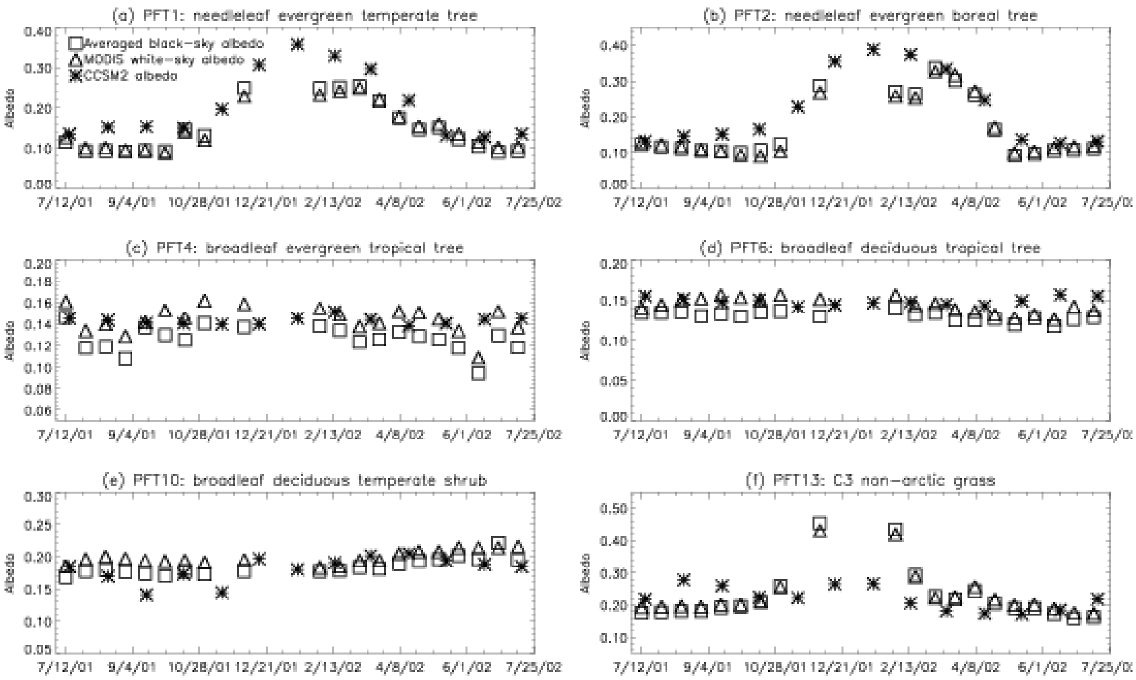

FIG. 3. The seasonal variation of the 16-day MODIS white-sky albedo, CCSM2 monthly averaged albedo, and 16-day averaged MODIS black-sky albedo over six grid cells with different dominant PFTs. (a) PFT 1: needleleaf evergreen temperate tree (51.6°N, 120.9°W); (b) PFT 2: needleleaf evergreen boreal tree (57.2°N, 120.9°W); (c) PFT 4: broadleaf evergreen tropical tree (4.2°S, 73.1°W); (d) PFT 6: broadleaf deciduous tropical tree (12.6°S, 53.4°W); (e) PFT 10: broadleaf deciduous temperate shrub (20.9°S, 123.8°E); and (f) PFT 13: C3 nonarctic grass (46.0°N, 115.3°E).

is fully consistent with the model albedo. The first term on the right represents the deviation of CCSM2 albedo from MODIS average albedo due to model deficiency in the albedo parameterization, while the second term reflects the inherent difference in computing monthly averaged albedo in the model versus MODIS white-sky albedo.

For comparison with model monthly average albedos, we need to average MODIS albedos over solar zenith angle. Such an averaging requires weighting the black-sky and white-sky albedos with their appropriate incident solar fluxes over the monthly and diurnal cycles. However, because such fluxes are not readily available, we are forced to introduce some approximations. First, we assume that the VIS and NIR solar fluxes are approximately the same. That they are not exactly the same has been noted by Oleson et al. (2003). Second, rather than combine black-sky and white-sky albedos from MODIS, we compute the diffuse albedo and average black-sky albedo separately, and we expect them to bound the MODIS average albedo that we would be able to derive with the use of incident solar fluxes. In other words, the last term in Eq. (6) is expected to be smaller in magnitude than the difference between the MODIS white-sky albedo and the average black-sky albedo that is obtained by weighting the black-sky albedos with the cosine of the solar zenith angle over the diurnal cycle at the point being considered. Note that the MODIS black-sky albedo is computed from Eq. (4) using the 16-day BRDF parameter products (MOD43C2) (version 003).

Figure 3 shows the seasonal variation of the CCSM2 albedo, MODIS average black-sky albedo, and MODIS white-sky albedo over six model grid cells with different dominant PFTs (see Table 2). Since the accuracy for MODIS albedos is evaluated to within ±0.02, differences smaller than that are not regarded as significant. For all six locations in Fig. 3, the differences between the MODIS white-sky albedo and the 16-day averaged black-sky albedo are usually very small (particularly under snow-free conditions). Further computations for July 2001 indicate that the differences are smaller than 0.01 (or 0.02) in magnitude in 46.7% (or 78.3%) of the global land grid cells between 60°S and 70°N (figure not shown). Hence, the MODIS white-sky albedo is generally sufficient (under the assumption of nearly equal downward solar fluxes for the VIS and NIR bands) to evaluate monthly averaged albedo from regional or global models.

For needleleaf evergreen trees in Fig. 3a, the CCSM2 albedo agrees with the MODIS data well in June and July, but is slightly larger than the MODIS data in August and September. This indicates that results in a particular month (e.g., results in July in Fig. 1c) are not necessarily indicative of results in other months. In Fig. 3b, the CCSM2 albedo is consistent with MODIS data during summer. For needleleaf evergreen trees in Figs. 3a and 3b, the model albedo is much higher than the MODIS data in winter months, which is consistent with Fig. 2c. For broadleaf evergreen trees (Fig. 3c), model and MODIS albedos agree with each other very well. These values are also consistent with in situ measurements (Oguntoyinbo 1970; Pinker et al. 1980; Shuttleworth et al. 1984).

Table 2. Location of 11 model grid cells with different dominant plant functional types (PFTs) along with their fractional area coverages. Each PFT is given in Table 1. PFTs 1, 2, and 4, 6, 10, and 13 are used in Fig.3, and PFTs 2 and 13 in Fig. 6. All PFTs are used in Fig. 7 and Table 3.

PFT	Area Coverage (%)	Center Lat/ Lon	Geographic Region
1	53	(51.6°N, 120.9°W)	Canada
2	61	(57.2°N, 120.9°W)	Canada
3	57	(62.8°N, 115.3°E)	Siberia
4	79	(4.2°S, 73.1°W)	Amazon
6	44	(12.6°S, 53.4°W)	Brazil
7	60	(37.6°N, 81.6°W)	United States
9	43	(40.5°N, 8.4°E)	Italy
10	100	(20.9°S, 123.8°E)	Australia
11	91	(65.6°N, 90.0°E)	Siberia
12	82	(57.2°N, 132.2°E)	Russia
13	98	(46.0°N, 115.3°E)	Mongolia

The abrupt drop of MODIS albedo in early June 2002 and the larger seasonal variation of MODIS albedo than model albedo are related to the consistent cloud cover over this area. For instance, the very anomalous MODIS albedo in early June was flagged as poor quality because of consistent cloud cover, and hence was estimated based on the MODIS back up magnitude inversion.

For broadleaf deciduous tropical trees (Fig. 3d), the CCSM2 albedo also agrees with MODIS data well. For broadleaf deciduous temperate shrub (Fig. 3e), the CCSM2 albedo is lower than the MODIS albedo from June to November. The relative large model versus MODIS albedo differences in September and November may be caused by the difference between the actual precipitation during these periods of the MODIS data and the 10-yr averaged model precipitation. In this location, the model leaf area index values in September and November are 0.2 and 0.11, respectively, and much of the model albedo comes from the underlying soil. The dry soil albedos specified for this grid box are 0.18 and 0.36 in the VIS and NIR bands, respectively, and the corresponding saturated soil albedos are 0.09 and 0.18, respectively. Therefore, the model albedo in September and November is very close to wet soil albedo. For C3 non-arctic grass (Fig. 3f), the CCSM2 albedo is slightly larger than the MODIS value in August and September, but it is smaller in other months. Because of a lack of snow at this location in the model (not shown), the CCSM2 albedo is much smaller than the MODIS value in December and January.

4. Evaluation of the solar zenith angle dependence of model albedo

In the previous section, we analyzed the global difference between MODIS white-sky albedo and CCSM2 monthly-averaged albedo. This difference is primarily caused by model deficiency in the treatment of land surface albedo, rather than by the inherent difference in computing model monthly averaged albedo and MODIS white-sky albedo. To better understand the results in Figs. 1 and 2, we further evaluate the four components of model albedo as well as their solar zenith angle dependence.

Hourly output of the four components of surface albedo was not saved in CCSM2 simulations. Therefore, we have run the CAM2/CLM2 to obtain this output. Global comparisons of model direct albedo with MODIS black-sky albedo at local solar noon averaged in July for the visible and near-infrared bands are shown in Figs. 4 and 5, respectively. Since direct albedo (as used by modelers) refers to the same quantity as black-sky albedo (as used by the MODIS team), hereafter we use direct albedo only in this section to avoid confusion.

Since NIR direct albedo $\left(\alpha_{N,d}\right)$ (Figs. 5a, b) is much larger than VIS direct albedo $\alpha_{v,d}$ (Figs. 4a, b) over snow-free surfaces, the model versus MODIS $\alpha_{N,d}$ difference (Fig. 5c) is larger in magnitude than the $\alpha_{v,d}$ difference (Fig. 4c) over most regions and the differences between the model monthly averaged albedo and MODIS white-sky albedo (Figs. 1c and 2c) is primarily contributed by the difference in Fig. 5c over most regions. For semiarid and arid regions, the model specifies visible soil albedos and then takes the NIR albedos as a factor of two larger. The actual ratio as given by MODIS is quite variable going from about 1.5 for the Chinese desert to well over 2 for some other deserts, possibly because this ratio is determined by the mineral content of the soil (Zhou et al. 2003). For instance, the model underestimates $\alpha_{N,d}$ by about 0.2 over the Sahara Desert (Fig. 5c), while it underestimates $\alpha_{v,d}$ by 0.02-0.1 (Fig. 4c). Over some regions (e.g., eastern China, southern Africa), the $\alpha_{v,d}$ difference in Fig. 4c and $\alpha_{N,d}$

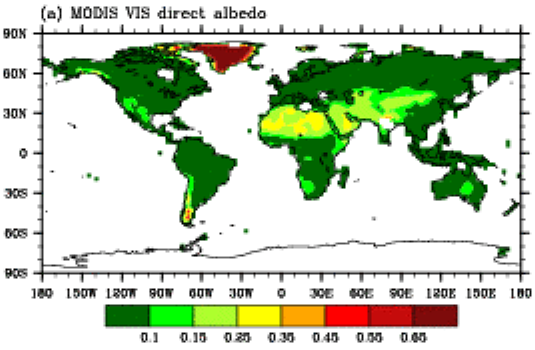
(a) MODIS VIS direct albedo

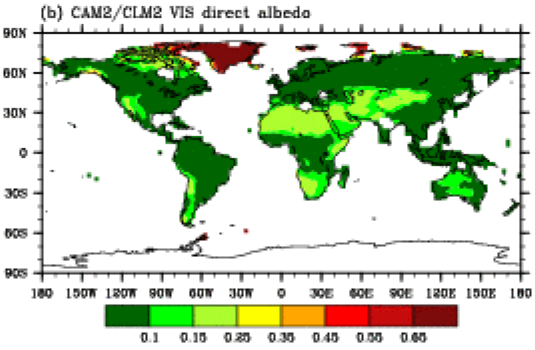
(b) CAM2/CLM2 VIS direct albedo

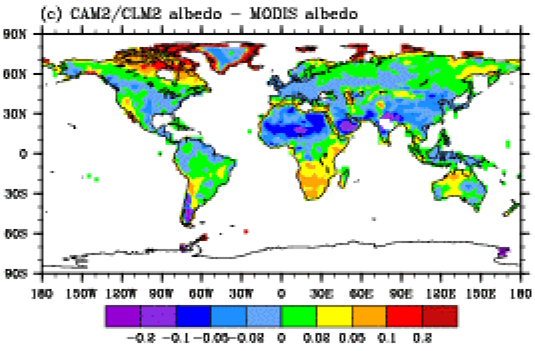
(c) CAM2/CLM2 albedo − MODIS albedo

FIG. 4. The global distribution of the CAM2/CLM2 direct albedo and MODIS direct albedo at local noon averaged in Jul 2001 for the visible (VIS) broad band.

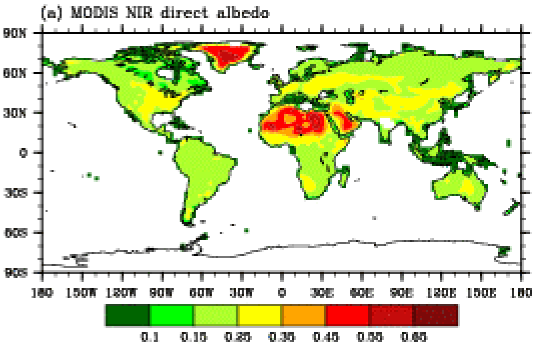
(a) MODIS NIR direct albedo

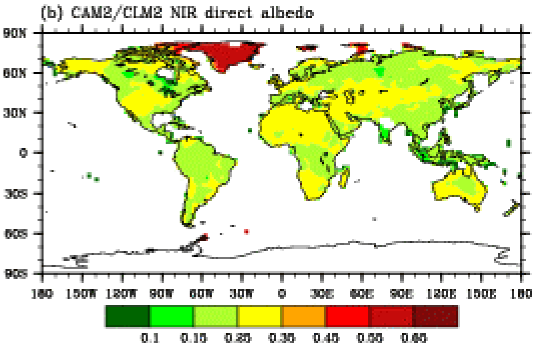
(b) CAM2/CLM2 NIR direct albedo

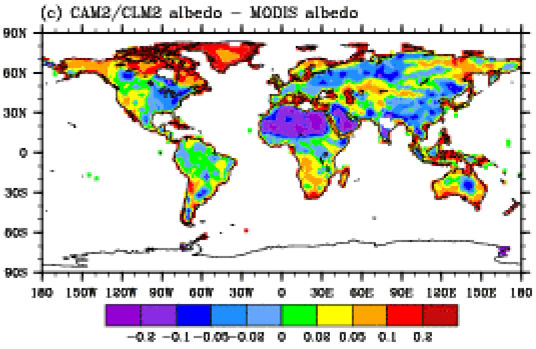
(c) CAM2/CLM2 albedo − MODIS albedo

FIG. 5. Same as Fig.4 except for the near-infrared (NIR) broad band.

in Fig. 5c are comparable in magnitude and are of the same sign. Over some other regions (e.g., most parts of Australia), these two differences are of opposite sign but the $\alpha_{N,d}$ difference is larger in magnitude. These conclusions are also supported by results in February over snow-free surfaces (not shown). For snow-covered regions, however, $\alpha_{v,d}$ is generally larger than $\alpha_{N,d}$, and the model versus MODIS $\alpha_{v,d}$ difference is as large as the $\alpha_{N,d}$ difference (not shown).

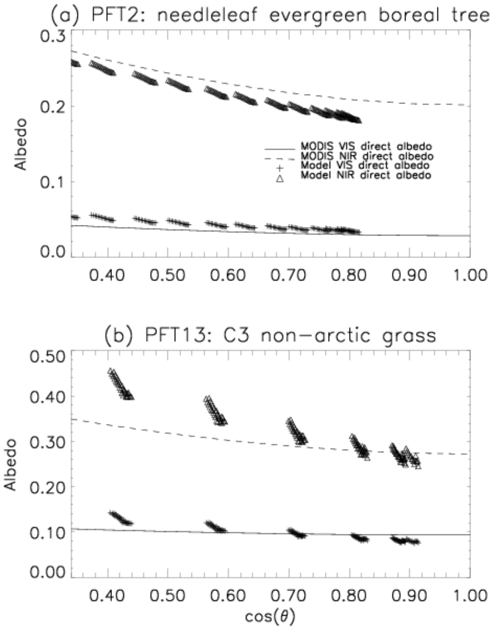

FIG. 6. Comparison of the solar zenith angle (θ) dependence between the CAM2/CLM2 hourly direct albedo and MODIS direct albedo for (a) PFT 2: needleleaf evergreen boreal tree (57.2°N, 120.9°W); and (b) PFT 13: C3 nonarctic grass (46.0°N, 115.3°E). Since the MODIS BRDF data at $\theta \geq 70°$ are not as reliable as at a lower θ, we show results with $\theta \leq 70°$ only. Model results are based on the CAM2/CLM2 hourly output for a 16-day period (12 - 27 July 2001). The MODIS direct albedo data are obtained from Eq. (4) using the MODIS BRDF parameters for the same period.

Next, we evaluate the solar zenith angle (SZA) dependence of the model albedo over 11 grid cells with different dominant PFTs and over different regions (Table 2). We only choose the grid cells without fractional covers for glacier, urban, wetland, and lake. The fractional covers for the dominant PFTs in 9 of the 11 grid cells are larger than 50%. They are larger than 40% in the other two grid cells (PFTs 6 and 9) because of the existence of four PFTs (each with more than 10 % area coverage) within each grid cell. Hourly output of the four components of CAM2/CLM2 albedo for a 16-day period (12 - 27 July 2001) are used. The model albedos fall in individual clusters that result from the sampling at the same hour but with seasonal variations changing the sun angle slightly from day to day. The MODIS direct albedo as a function of θ is obtained from Eq. (4) using the MODIS BRDF parameters for the same location and period.

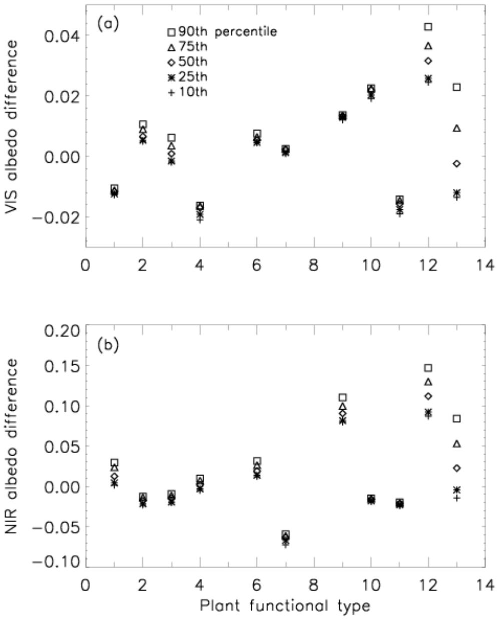

FIG. 7. The 10th, 25th, 50th, 75th, and 90th percentiles of the differences between the CAM2/CLM2 hourly direct albedo and MODIS direct albedo (a) in the VIS band; and (b) in the NIR band for the 11 grid cells with different dominant PFTs (see Table 2).

Results are shown in Fig. 6 for PFT 2 (needleleaf evergreen boreal tree) and PFT 13 (C3 nonarctic grass). For SZA larger than 70°, the input surface reflectances for retrieval are usually poor, and the polynomial representation in Eq. (4) is not as good either (Lucht et al. 2000a). Therefore, our discussions are limited to SZA less than 70°.

Figure 6 shows that both model and MODIS direct albedos decrease monotonically with $\cos\theta$. However, the model direct albedo increases too fast with the increase of SZA (or with the decrease of $\cos\theta$). This is also the case for most PFTs in Table

2. The model overestimates VIS direct albedo and underestimates NIR direct albedo for PFT 2 (Fig. 6a). The model (VIS and NIR) direct albedo is closer to the MODIS albedo at local noon (i.e., at a higher $\cos\theta$) than in the morning or afternoon for PFT 13 (Fig. 6b). We have also chosen four different grid cells with the dominant vegetation being PFT 2 or PFT 13, and the SZA dependence is quite similar to those in Fig. 6 (not shown).

Table 3. The median difference between the CAM2/CLM2 hourly direct albedo and MODIS direct albedo for a 16-day period (12-27 July 2001) and the difference between the model diffuse albedo and MODIS white-sky albedo for the same period in the VIS and NIR bands for the 11 grid cells with different dominant PFTs (see Table 2).

PFT	Median direct albedo Difference		Diffuse albedo difference	
	VIS	NIR	VIS	NIR
1	-0.01	0.01	0.00	0.06
2	0.01	-0.02	0.02	0.02
3	0.00	-0.01	0.01	0.02
4	-0.02	0.00	-0.01	0.05
6	0.01	0.02	0.02	0.07
7	0.00	-0.06	0.01	-0.02
9	0.01	0.09	0.02	0.13
10	0.02	-0.02	0.02	-0.04
11	-0.02	-0.02	-0.01	0.02
12	0.03	0.11	0.05	0.17
13	0.00	0.02	0.03	0.09

Figure 7 shows the 10th, 25th, 50th, 75th, and 90th percentiles of the differences between the model and MODIS direct albedos for the 11 grid cells in Table 2. The 50th percentiles (or median differences) are also given in Table 3 for convenience. The difference between the model VIS direct albedo and MODIS data is between 0.02 and 0.03 in magnitude for PFTs 4 and 10-12, and is less than 0.02 in magnitude for the other seven cells (Table 3). In contrast, the difference for the NIR band is between 0.06 and 0.11 in magnitude for PFTs 7, 9, and 12, and is equal to or less than 0.02 in magnitude for the other eight cells (Table 3). Figure 7a shows that the difference between the 90th and 10th percentiles for the VIS band is less than 0.02 for all grid cells except for PFT 13, while Fig. 7b demonstrates that the corresponding difference for the NIR band is less than 0.02 for only six cells (PFTs 2-4, 7, 10, and 11), and is as large as 0.1 for PFT 13 and 0.07 for PFT 12.

The model diffuse albedo and MODIS white-sky albedo are independent of $\cos\theta$, and their differences in the VIS and NIR bands for the 11 grid cells in Table 2 are given in Table 3. The CAM2/CLM2 diffuse albedos usually have a higher bias (in magnitude) compared to that of MODIS in the median comparison. Since the diffuse albedo integrates over the upward hemisphere [e.g., Eq. (5)], it has large contributions from sky near the horizon, where direct albedos are generally higher (e.g., Fig. 6), approximately half from zenith angles greater than 60°. In contrast, for PFT 2 or 13 in Fig. 6, the median direct albedo difference for the VIS or NIR band corresponds to a solar zenith angle of about 45°. Note that the computation of diffuse albedo in the two-stream method (Bonan 1996) is somewhat different from the computation of MODIS white-sky albedo in Eq. (5). Therefore, even though the model NIR direct albedo is lower than the MODIS NIR direct albedo for PFT 2 in Fig. 6a, the corresponding model diffuse albedo is actually higher than the MODIS white-sky albedo (Table 3).

5. The solar zenith angle dependence of desert albedo

Most land surface models assume that the bare soil albedo is a function of soil color and moisture but independent of SZA. However, analyses of the MODIS BRDF and albedo data over thirty desert locations indicate that bare soil albedo does vary with SZA. This is confirmed using in-situ data. The global 0.05° MODIS BRDF and albedo Climate Modeling (CMG) data (version 4) are used in this section. Only the data derived primarily from full inversion under snow-free condition are used. Further, we only analyze the BRDF data for the 16-day periods starting from Julian days in 2001: 001, 033, 065, 097, 129, 161, 193, 225, 257, 289, 321, and 353. During these periods, we have identified thirty 0.05° pixels over different desert areas with zero fractional vegetation cover to examine the SZA dependence of bare soil albedo. These pixels are selected to represent each of the major deserts of the world.

At each pixel, the black-sky albedo and its SZA dependence do not change much during the twelve 16-day periods. For each location, there is a median albedo among twelve 16-day periods at each SZA, so a curve can be obtained from median albedos over all SZAs. Figure 1a,b shows these median SZA dependence curves of black-sky albedo over all thirty pixels. The significant geographic variation of desert albedo is consistent with previous studies (*Tsvetsinskaya et al.*, 2002). For instance, the IQRs of the black-sky albedos at 60° SZA are 0.067 and 0.130 in the VIS and NIR bands, respectively. To see the SZA dependence more clearly, we normalize each curve in Fig. 8a,b by its value at 60° SZA, and results are shown in Fig. 8c,d. While the albedo increases with SZA over each pixel, its variation with SZA is quantitatively different over different pixels.

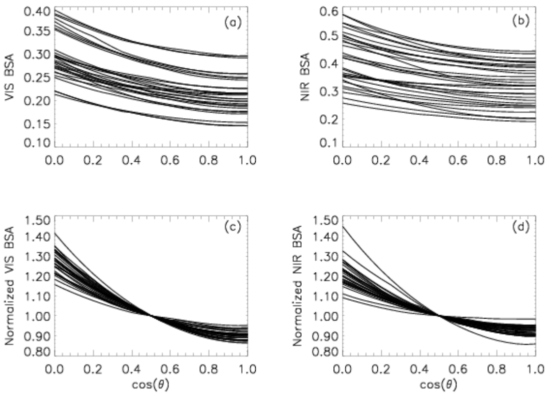

Fig. 8 The median curves of the MODIS black-sky albedos for the VIS band in (a) and NIR band in (b) versus the cosine of SZA at 30 desert locations. The normalized curves with respect to their albedo values at 60° SZA are shown for the VIS band in (c) and NIR band in (d).

To adequately describe the SZA dependence of bare soil albedo as given in Fig. 1, a new albedo formulation is derived here using the MODIS BRDF/albedo algorithm and data (Schaaf et al. 2002; Lucht et al. 2000 a,b):

$$\alpha(\theta)=\alpha_r\cdot\left\{1+C_1\cdot\left[g_1(\theta)-g_1(60^\circ)\right]+C_2\cdot\left[g_2(\theta)-g_2(60^\circ)\right]\right\} \quad (7)$$

where α is the black-sky albedo, θ is solar zenith angle, α_r is the albedo at 60° SZA and depends on season and location. The functions g_1 and g_2 are from the MODIS algorithm:

$$g_1(\theta)=-0.007574-0.070987\theta^2+0.307588\theta^3$$

and

$$g_2(\theta)=-1.284909-0.166314\theta^2+0.04184\theta^3$$

The parameters C_1 and C_2 are the ratios of the volumetric and geometric parameters in the MODIS algorithm (Schaaf et al. 2002) over α_r, respectively. Figure 9a-d shows these parameters in VIS and NIR bands for thirty pixels as a function of α_r. Based on this figure, we obtain $C_1 = 0.335$ and $C_2 = 0.070$.

We have also tested the simple formulation (*Briegleb et al.*, 1986):

$$\alpha(\theta)=\alpha_r\cdot\frac{1+C}{1+2C\cdot\cos\theta} \quad (8)$$

where the empirical parameter C was taken as 0.4 for arable grass, grassland and desert, and 0.1 for all other types (*Briegleb et al.*, 1986). Equation (8) and the above C values have also been used in the remote sensing retrieval of land surface solar fluxes (*Pinker et al.*, 1992) and in some land-atmosphere coupled models (e.g., *Hou et al.*, 2002).

A more appropriate C value can be determined by fitting each curve in Fig. 8a,b to Eq. (8) by minimizing the integral over all SZA's for each 16-day period:

$$V=2\int_{\theta=0}^{\pi/2}\cos\theta\cdot\sin\theta\cdot\left(\alpha_M-\alpha_C\right)^2 d\theta \quad (9)$$

where α_M is the MODIS albedo and α_c is the computed from (8). The weighting factor of cosθ is the same as that used for computing the white-sky albedo (Schaaf et al. 2002). This is chosen also because MODIS data are more reliable at SZA less than 70° and because the albedo is more important at a smaller SZA when solar flux itself is large. The C values for all thirty pixels are plotted as a function of α_r in Fig. 9e,f. Their mean values of VIS and NIR bands are 0.18 and 0.12, respectively, and their average of 0.15 is used for both bands to be consistent with *Briegleb et al.* (1986). Furthermore, the best-fit linear equations can be obtained:

$$C_{vis}(\alpha_r)=0.28-0.44\alpha_r \qquad \text{and}$$

$$C_{nir}\left(\alpha_r\right) = 0.12 - 0.01\alpha_r$$

The outlier at the top in VIS and NIR bands locate at the same location (30.525°S, 69.725°W), and corresponds to the top line in Fig. 1c,d. To compare the performance of (7) and (8), we compute $d = \left(\frac{1}{30} \sum_{i=1}^{30} V_i \right)^{1/2}$, where V_i is computed from (9) for each of the 30 pixels. The values of d are 0.0063, 0.0085, and 0.0076 using the two-parameter model, one-parameter model with constant C as well as the best-fit linear equations, respectively. This shows that the two-parameter model is a little better than the one-parameter model. If the white-sky albedo is used (i.e., without considering the SZA dependence), the d value would be 0.0197 and is much bigger than those using (7) or (8). This indicates the importance of the SZA dependence. Figure 9g,h evaluates the SZA dependence over a pixel (19.975°N, 43.325°E) using (7) and (8) with different C values. The simulated SZA dependence using the two-parameter, one-parameter model with the best-fit linear equation or the C value fixed at 0.15 are consistent with the MODIS data for SZA less than 60°. In contrast, the albedo computed with C=0.4 increases with SZA much faster than indicated by the MODIS data, and its value at zero SZA is lower by 0.03 for the VIR band and 0.05 for the NIR band.

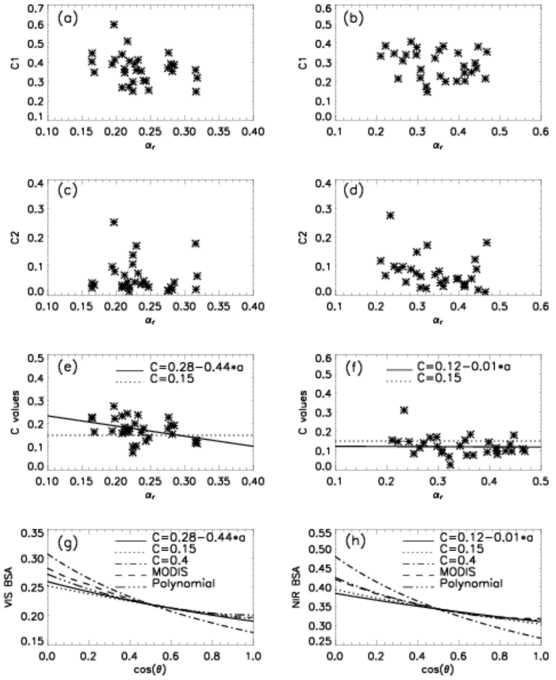

Fig. 9 The median C_1 versus the MODIS black-sky albedos at 60° SZA (α_r) for 30 pixels in VIS band in (a) and NIR band in (b). The median C_2 versus α_r in VIS band in (c) and NIR band in (d). The *C* values versus α_r in VIS band in (e) and NIR band in (f) (solid line: the best-fit linear function, dotted line: the average C value of VIS and NIR bands). (g) The SZA dependence at a pixel (19.975°N, 43.325°E) using the MODIS data directly and computed using (1) and (2) with different C values (the best-fit linear function or fixed values) in the VIS band; (h) Same as (g) except in the NIR band.

Based on these analyses, we recommend the use of the polynomial Eq. (7) or Eq. (8) with C = 0.15 over bare soil in land modeling and remote sensing retrieval of land surface solar fluxes. Then the white-sky albedo can be obtained analytically by integrating Eqs. (7) and (8) over all SZA's [using the weighting factor in (9)], and is $\alpha_{ws} = 0.97\alpha_r$ for (7) and $\alpha_{ws} = 0.96\alpha_r$ for (8).

6. Conclusions and further discussions

Land surface albedo directly affects surface energy and water balance. Monthly averaged albedo represents the ratio of the total reflected to incoming solar radiation, and is one of the standard output variables from global models. The recent availability of the MODIS BRDF/albedo data makes it possible to evaluate and improve the treatment of albedos in global models. However, the way model time-averaged albedo is computed is different from the way satellite white-sky albedo is obtained. Through the analysis of MODIS white-sky and black-sky albedo data, this difference is found to yield relatively small inherent differences in model-averaged albedo and MODIS white-sky albedo. In other words, under the condition of nearly equal downward solar fluxes for the VIS (with wavelength $\lambda < 0.7\mu m$) and NIR ($\lambda > 0.7\mu m$) bands, the MODIS white-sky albedo can be, to a large degree, used directly to evaluate monthly averaged model albedo values over snow-free grid cells.

The difference between the monthly averaged albedo from the NCAR CCSM2 versus the MODIS white-sky albedo in February and July is within 0.02 or statistically insignificant over about 40% of the global land between 60°S and 70°N (e.g., tropical forests). However, the model significantly underestimates albedo throughout the whole year over deserts (e.g., the Sahara Desert). The model versus MODIS albedo difference can also be larger than 0.05 over some other regions, particularly over semiarid regions (e.g., Australia). These results are consistent with the previous study of Wei et al. (2001) in which the BATS and LSM models were found to contain significant errors in albedos over desert and semidesert regions and winter snow compared with the AVHRR data.

To better understand these differences, we have carried out simulations using the CAM2/CLM2 (which represent the atmospheric and land components of the CCSM2) and saved the hourly output of the four components of model albedo, including the direct and diffuse albedos for the VIS and NIR broad bands. Then, the model direct albedos at local noon for the VIS and NIR broad bands were evaluated using the MODIS direct (i.e., black-sky) albedo data. Because the NIR direct albedo ($\alpha_{N,d}$) is usually much larger than the VIS direct albedo ($\alpha_{v,d}$) over snow-free surfaces, the $\alpha_{N,d}$ difference between CAM2/CLM2 and MODIS is found to be larger than the $\alpha_{v,d}$ difference over most snow-free regions (e.g., the Sahara Desert). However, over some regions, these differences may be of comparable magnitude with the same signs (e.g., over southern Africa) or opposite signs (e.g., over part of Australia).

We have also selected 11 grid cells with different dominant plant functional types to evaluate the solar zenith angle dependence of the CAM2/CLM2 albedo. Model diffuse albedo in the NIR band is found to be larger by 0.05 or more than the MODIS white-sky albedo over five of these grid cells. In contrast, its difference from the MODIS data in the VIS band is within 0.02 in magnitude in nine of these cells. Both MODIS and model direct albedos generally increase with the increase of solar zenith angle. However, model direct albedo usually increases faster than MODIS data over most of these grid cells, resulting in a larger black-sky albedo difference between model and MODIS in the morning or afternoon than at local noon.

These albedo differences between CCSM2 (or CAM2/CLM2) and MODIS are related to the deficiencies in the model simulation of snow cover and soil moisture and in the model's specification of leaf and stem area indexes, as explored in a complementary study (Zhou et al. 2003). The LAI and SAI of CLM2 are tightly linked to the magnitude of the albedo biases primarily over snow-covered regions because of the use of LAI and SAI in computing the fraction of canopy covered by snow (Zhou et al. 2003). For snow-free regions, LAI and SAI could also be important over thin canopies if the canopy and soil albedos are quite different. PFTs used in the CCSM2 were based on the global 1-km land cover data, as derived from the AVHRR data (Bonan et al. 2002b). Since these land cover data are somewhat different from the MODIS land cover data, the misclassification of land cover type may also contribute to the albedo difference between the model and MODIS data. Over regions with consistent cloud cover, the albedo difference between the model and MODIS data may also be partially caused by the uncertainty of the MODIS data based on the magnitude (rather than full) inversion. The albedo biases are also partially caused by the deficiency of the two-stream method used to compute albedo in the model. The two-stream approximation does not include the effect of three-dimensional structure in vegetation on the radiative transfer that is important for the computation of the land surface albedo and the percentage of solar radiation absorbed by the canopy. The preceding analyses combined with the MODIS BRDF albedo data provide a starting point towards developing a BRDF-based treatment of radiative transfer through canopy for land surface models that can realistically simulate the mean albedo and the solar zenith angle dependence of albedo.

Our analyses of the MODIS and in-situ data indicate that bare soil albedo depends on the SZA, and this dependence can be adequately represented by Eq. (7) with $C_1 = 0.335$ amd $C_2 = 0.070$ as well as Eq. (8) with $C = 0.15$. These dependences need to be considered in land surface modeling. Further work is also needed to evaluate the impact of these formulations on the remote sensing retrieval of land surface solar fluxes.

Acknowledgments. This work was supported by NASA through its EOS IDS Program (429-81-22; 428-81-22). The first three authors were also supported by NOAA under grant NA06GP0569. Dr. Steve Mullen is thanked for helpful comments. We especially thank three reviewers for detailed and insightful comments, which significantly improved the clarity of our presentation.

References

Blackmon, M., and Coauthors, 2001: The Community Climate System Model. *Bull. Amer. Meteor. Soc.*, **82**, 2357-2376.

Bonan, G. B., 1996: A land surface model (LSM version 1.0) for ecological, hydrological, and atmospheric studies: Technical description and user's guide. NCAR Tech. Note NCAR/TN-417 + STR, 150 pp.

—, S. Levis, L. Kergoat, and K. W. Oleson, 2002a: Landscapes as patches of plant functional types: an integrating concept for climate and ecosystem models. *Global Biogeochem. Cycles*, **16**, 1021, doi 10.1029/2000GB001360.

—, B., K. W. Oleson, M. Vertenstein, S. Levis, X. Zeng, Y. Dai, R. E. Dickinson, and Z. L. Yang, 2002b: The land surface climatology of the Community Land Model coupled to the NCAR Community Climate Model. *J. Climate*, **15**, 3123-3149.

Briegleb, B. P., P. Minnis, V. Ramanathan, and E. Harrison 1986: Comparison of regional clear sky albedos inferred from satellite observations and model calculations, *J. Clim. Appl. Meteorol.*, **25**, 214-226.

Csiszar, I., and G. Gutman, 1999: Mapping global land surface albedo from NOAA AVHRR. *J. Geophys. Res.*, **104**, 6215-6228.

Dai, Y., and Coauthors, 2003: The Common Land Model. *Bull. Amer. Meter. Soc.*, **84**, 1013-1023.

Dickinson, R. E., and A. Henderson-Sellers, 1988: Modeling tropical deforestation: A study of GCM land-surface parameterizations. *Quart. J. Roy. Meteor. Soc.*, **114**, 439- 462.

—, A. Henderson-Sellers, and P. J. Kennedy, 1993: Biosphere-Atmosphere Transfer Scheme (BATS) Version le as coupled to the NCAR Community Model. NCAR Tech. Note NCAR/TN-387 + STR, 72 pp.

Dorman, J. L., and P. J., Sellers, 1989: A global climatology of albedo, roughness length and stomatal resistance for atmospheric general circulation models as represented by the simple biosphere model (SiB). *J. Appl. Meteor.*, **28**, 833-855.

Guenther, B., X. Xiong, W. Salomonson, W. L. Barnes, and J. Young, 2002: On-orbit performance of the Earth Observing System Moderate Resolution Imaging Spectroradiometer; first year of data. *Remote Sens. Environ.*, **83**, 16-30.

Hou, Y. T., Moorthi, S., and Campana, K. 2002: Parameterization of solar radiation transfer in the NCEP models, NCEP Office Note 441, 34.

Jin, Y., C. B. Schaaf, F. Gai, X. Li, A. Strahler, X. Zeng, and R. E. Dickinson, 2002: How does snow impact the albedo of vegetated land surfaces as analyzed with MODIS data? *Geophys. Res. Lett.*, **29**, NO. 10, 10.1029/2001GL014132.

—, —, —, —, —, W. Lucht, and S. Liang, 2003: Consistency of MODIS surface BRDF/Albedo retrievals: 2. Validation. *J. Geophys. Res.*, **108**(D5), 4159, doi:10.1029/2002JD002804.

Justice, C. O., J. R. G. Townshend, E. F. Vermote, E. Masuoka, R. E. Wolfe, N. Saleous, D. P. Roy, and J. T. Morisette, 2002: An overview of MODIS land data processing and product status. *Remote Sens. Environ.*, **83**, 3-15.

Liang, S., A. H. Strahler, and C. W. Walthall, 1999: Retrieval of land surface albedo from satellite observations: A simulation study. *J. Appl. Meteor.*, **38**, 712-725.

—, and Coauthors, 2002: Validating MODIS land surface reflectance and albedo products: Methods and preliminary results. *Remote Sens. Environ.*, **83**, 149-162.

Lucht, W., C. B. Schaaf, and A. H. Strahler, 2000a: An algorithm for the retrieval of albedo from space using semiempirical BRDF models. *IEEE Trans. Geosci. Remote Sens.*, **38**, 977-998.

—, A. H. Hyman, A. H. Strahler, M. J. Barnsley, P. Hobson, and J.-P. Muller, 2000b: A comparison of satellite-derived spectral albedos to ground-based broadband albedo measurements modelled to satellite spatial scale for a semi-desert landscape. *Remote Sens. Environ.*, **74**, 85-98.

Monteith, J. L., 1973: *Principles of Environmental Physics*. Edward Arnold, 241 pp.

Oguntoyinbo, J. S., 1970: Reflection coefficient of natural vegetation, crops and urban surface in Nigeria. *Quart. J. Roy. Meteor. Soc.*, **96**, 430-441.

Oleson, K. W., G. B. Bonan, C. Schaaf, F. Gao, Y. Jin, and A. Strahler, 2003: Assessment of global climate model land surface albedo using MODIS data. *Geophys. Res. Lett.*, **30**, 1443, doi:10.1029/2002GL016749.

Pinker, R. T., O. E. Thompson, and T. F. Eck, 1980: The albedo of a tropical evergreen forest. *Quart. J. Roy. Meteor. Soc.*, **106**, 551-558.

— and I. Laszlo 1992: Modeling of surface solar irradiance for satellite applications on a global scale, *J. Appl. Meteorol.*, **31**, 194-211.

Ross, J. K., 1981: *The Radiation Regime and Architecture of Plant Stands*. Dr. W. Junk Publishers, 392 pp.

Roujean, J. L., M. Leroy, and P. Y. Deschamps, 1992: A bidirectional reflectance model of the Earth's surface for the correction of remote sensing data. *J. Geophys. Res.*, **97**, 20 455-20 468.

Schaaf, C. B., and Coauthors, 2002: First operational BRDF, albedo nadir reflectance products from MODIS. *Remote Sens. Environ.*, **83**, 135-148.

Shuttleworth, W. J., and Coauthors, 1984: Observations of radiation exchange above and below Amazonian forest. *Quart. J. Roy. Meteor. Soc.*, **110**, 1163-1169.

Strugnell, N., and W. Lucht, 2001: Continental-scale albedo inferred from AVHRR data, land cover class and field observations of typical BRDFs. *J. Climate*, **14**, 1360-1376.

—, —, and C. B. Schaaf, 2001: A global albedo data set derived from AVHRR data for use in climate simulations. *Geophys. Res. Lett.*, **28**, 191-194.

Tsvetsinskaya, E. A., C. B. Schaaf, F. Gao, A. H. Strahler, R. E. Dickinson, X. Zeng, and W. Lucht, 2002: Relating MODIS derived surface albedo to soils and rock types over Northern Africa and the Arabian peninsula. *Geophys. Res. Lett.*, **29**, 1353, doi:10.1029/2001GL014096.

Wei, X., A. Hahmann, R. E. Dickinson, Z.-L. Yang, X. Zeng, K. Schaudt, C. Schaaf, and N. Strugnell, 2001: Comparison of albedos computed by land surface models and evaluation against remotely sensed data. *J. Geophys. Res.*, **106**, 20 687-20 702.

Wiscombe, W. and S. G. Warren, 1980: A model for the spectral albedo of snow, I: Pure Snow. *J. Atmos. Sci.*, **37**, 2712-2733.

Wolfe, R. E., and Coauthors, 2002: Achieving sub-pixel geolocation accuracy in support of MODIS land science. *Remote Sens. Environ.*, **83**, 31-49.

Zeng, X., M. Shaikh, Y. Dai, R. E. Dickinson, and R. B. Myneni, 2002: Coupling of the Common Land Model to the NCAR Community Climate Model. *J. Climate*, **14**, 1832-1854.

Zhou, L., and Coauthors, 2003: Comparison of seasonal and spatial variations of albedos from Moderate-Resolution Imaging Spectroradiometer (MODIS) and Common Land Model. *J. Geophys. Res.*, **108,** 4488, doi:10.1029/2002JD003326.